Control of dynamic cell behaviors during angiogenesis and anastomosis by Rasip 1

Minkyoung Lee[1,3], Charles Betz[1], Ilkka Paatero[1,4], Niels Schellinx[1], Jianmin Yin[1], Christopher William Wilson[2,5], Weilan Ye[2], Markus Affolter[1,*] and Heinz-Georg Belting[1,*]

[1] Department of Cell Biology, Biozentrum, University of Basel, Klingelbergstrasse 70, 4056 Basel, Switzerland.

[2] Department of Molecular Biology, Genentech, Inc., South San Francisco, CA, USA.

[3] Current address: Department of Biosystems Science and Engineering, ETH Zurich, Mattenstrasse 26, 4058 Basel, Switzerland.

[4] Current address: Turku Centre for Biotechnology, University of Turku and Åbo Akademi University, Turku, 20520, Finland.

[5] Current address: Novartis Institutes for BioMedical Research, Cambridge, MA 02139, USA

[*]Correspondence: markus.affolter@unibas.ch (M.A.), heinz-georg.belting@unibas.ch (H.-G.B.)

Abstract

Organ morphogenesis is driven by a wealth of tightly orchestrated cellular behaviors, which ensure proper organ assembly and function. Many of these cell activities involve cell-cell interactions and remodeling of the F-actin cytoskeleton. Here, we analyze the requirement for Rasip1 (Ras-interacting protein 1), an endothelial-specific regulator of junctional dynamics, during blood vessel formation. Phenotype analysis of *rasip1* mutants in zebrafish embryos reveal distinct requirements for Rasip1 during sprouting angiogenesis, vascular anastomosis and lumen formation. During angiogenic sprouting, Rasip1 is required for efficient cell pairing, which is essential for multicellular tube formation. High-resolution time-lapse analyses show that these cell pairing defects are caused by a destabilization of tricellular junctions suggesting that tri-cellular junctions may serve as a counterfort to tether sprouting endothelial cells during morphogenetic cell rearrangements. During anastomosis, Rasip1 is required to establish a stable apical membrane compartment; *rasip1* mutants display ectopic, reticulated junctions and the apical compartment is frequently collapsed. Loss of Ccm1 and Heg1 function leads to junctional defects similar to those seen in *rasip1* mutants. Analysis of *radil-b* single and *rasip1/radil-b* double mutants reveal distinct and overlapping functions of both proteins. While Rasip1 and Radil-b have similar functions during angiogenic sprouting, the junction formation during anastomosis may primarily depend on Rasip1.

Keywords

Zebrafish, Endothelial cells, Angiogenesis, Anastomosis, VE-cadherin, Rasip1

44 # Introduction

45

46 The cardiovascular system is the first organ to become functional during embryonic
47 development. The generation of vascular networks is essential for developmental
48 patterning, growth and survival of the vertebrate embryo. As the embryo grows, the
49 vasculature adjusts to the increasing demand of nutrients and oxygen by an expansion
50 of the vasculature tree via sprouting angiogenesis, vascular remodeling and
51 adaptation of blood vessel diameter. Vascular morphogenesis is driven by a wealth of
52 dynamic cellular behaviors, which are regulated by molecular as well as physical cues,
53 and are characterized by an extraordinary plasticity (Adams and Alitalo, 2007;
54 Baeyens et al., 2016; Duran et al., 2017). At the cellular level, blood vessel
55 morphogenesis and remodeling are accomplished by endothelial cell behaviors
56 including cell migration, cell rearrangement and cell shape changes (Betz et al., 2016).
57 This repertoire of dynamic behaviors allows endothelial cells to rapidly respond to
58 different contextual cues, for example during angiogenic sprouting, anastomosis,
59 pruning, diapedesis or regeneration.
60 Previous studies have shown that vascular tube formation requires extensive and
61 diverse cell shape changes and that these changes can be driven by junctional
62 remodeling as well as dynamic regulation of the cortical actin cytoskeleton (Gebala et
63 al., 2016; Paatero et al., 2018; Phng et al., 2015; Sauteur et al., 2014). Junctional
64 remodeling is essential for cell rearrangements, which drive multicellular tube
65 formation. Enlargement of the luminal space, on the other hand, requires apical
66 membrane invagination (Barry et al., 2016; StriliC et al., 2009). During anastomosis,
67 the apical membrane can invaginate through the entire cell leading to the formation of
68 a unicellular tube (Lenard et al., 2013).

69 Junctional remodeling and membrane invagination rely on the dynamic regulation of
70 the F-actin cytoskeleton at the endothelial cell junction and apical cortex, respectively.
71 Small GTPases of the Rho family, including Cdc42, Rac1 and RhoA are essential
72 regulators of F-actin dynamics and have been shown to play critical roles during blood
73 vessel formation *in vitro* and *in vivo* (reviewed by (Barlow and Cleaver, 2019). In the
74 vasculature, these GTPases are partially regulated by the adaptor protein Rasip1.
75 Rasip1 has been shown to promote Rac1 and Cdc42 activity, whereas it inhibits RhoA
76 activity by binding to the GTPase activating protein Arhgap29 (Barry et al., 2016; Xu
77 et al., 2011). Ablation of Rasip1 in mice and knock-down of *rasip1* zebrafish cause
78 severe vascular defects (Wilson et al., 2013; Xu et al., 2011). During vasculogenesis,
79 Rasip1 is required for the lumenization of the dorsal aorta, in particular for the clearing
80 of apical membrane compartments from junctional proteins and for the opening of the
81 vascular lumen between endothelial cells (Barry et al., 2016). However, the role of
82 Rasip1 during sprouting angiogenesis and anastomosis has not been studied in detail.
83 To gain more insight into the cellular and molecular mechanisms of vascular tube
84 formation during angiogenesis, we have generated loss-of-function alleles in the
85 zebrafish *rasip1* gene and performed high-resolution time-lapse imaging to observe
86 junctional dynamics during sprouting angiogenesis and anastomosis. Loss of *rasip1*
87 causes multiple vascular defects, with respect to angiogenic sprouting, including
88 defects in cell proliferation, junctional stability and lumen formation. Furthermore,
89 analyses of *radil-b* and *rasip1;radilb* double mutants reveal partly redundant roles for
90 the two proteins. Lastly, knock-down of *ccm1* and *heg1* phenocopies the apical
91 junctional defects seen in *rasip1*, suggesting a functional interaction between the
92 proteins during blood vessel formation.

93 # Results

94

95 **Loss of Rasip1 function causes broad vascular defects**

96 To investigate the role of Rasip1 in vascular morphogenesis we employed
97 CRISPR/Cas9 technology to generate several mutant alleles, namely *rasip1*^{ubs23},
98 *rasip1*^{ubs24} and *rasip1*^{ubs28}, respectively (S-Figure 1). The *rasip1*^{ubs28} allele comprises
99 a deletion of about 35kb including the *rasip1* coding region from exon 3 to 16, encoding
100 a severely truncated protein lacking the Ras-association, Forkhead-association and
101 Dilute domains (Figure 1a). Since the truncated protein lacks all the conserved
102 domains, we consider *rasip1*^{ubs28} to be a null-allele and focused our studies on the
103 analysis of this mutant.

104 Homozygous *rasip1* mutants displayed hemorrhages and vascular instability in the
105 cranial vasculature at 3 days of development (Figure 1b,c). Furthermore, we observed
106 transient pericardial edema between 3 and 5 dpf (Figure 1d), which usually
107 disappeared during larval development. In the trunk, *rasip1* mutants showed reduced
108 blood flow, which correlated with irregular and generally reduced diameter of the
109 dorsal aorta (DA) and intersegmental vessels (ISVs) (Figure 1e-g). These differences
110 were transient and by 5 dpf the average vessel diameter had recovered to normal size.
111 Despite these severe defects, homozygous *rasip1* mutants recovered and about 30%
112 of them developed to fertility.

113

114 **Reduced motility and proliferation during angiogenic sprouting in *rasip1***
115 **mutants**

116 To find out whether the loss of *rasip1* may affect dynamic cell behaviors, we performed
117 time-lapse analyses, concentrating on the developing ISVs. ISVs sprouts emerge from

118 the DA at about 22-24 hpf and extend towards the dorsal side of the embryo. In wild-
119 type embryos, they reach the dorsal part of the neural tube by 28 hpf and initiate
120 formation of the dorsal longitudinal anastomotic vessel (DLAV) (Lawson and
121 Weinstein, 2002). In our time-lapse movies we observed that by 30 hpf almost all
122 sprouts in the trunk region had completed dorsal sprouting and engaged in contact
123 with neighboring sprouts (S-Figure 2a, b). In contrast, ISV sprouting in *rasip1* mutants
124 appeared sluggish and 25% of sprouts were incomplete by 30 hpf (S-Figure 2a, b). To
125 see whether stunted outgrowth was reflected by a difference in the number of
126 endothelial cells contributing to ISV sprouts, we counted nuclei within each sprout at
127 30 hpf (S-Figure 2c). In wild-type and *rasip1* mutants, the number ISV nuclei was quite
128 variable ranging between one and five. However, we observed a clear enrichment of
129 ISVs containing one or two nuclei in mutants when compared to wild-type, which
130 contained three to four nuclei. To differentiate whether this diminished cell number
131 was caused either by reduced recruitment or by proliferation defects of endothelial
132 cells, we tracked endothelial cell nuclei during ISV formation (S-Figure 2d-g). In wild-
133 type siblings, we observed that two cells migrated from the DA into the sprout,
134 undergoing one round of division each thus giving rise to an ISV consisting of four
135 cells (S-Figure 2e); ISVs comprising three cells were usually formed by two migrating
136 cells and a single cell division (S-Figure 2f). In *rasip1* mutants we rarely observed cell
137 divisions within the sprouts (S-Figure 2d, g). Instead, most cells in the sprout originated
138 from the DA and occasionally we observed three cells migrating into the sprout (Figure
139 2f). Hence, these results show that proliferation in sprouting endothelial cells is
140 reduced in *rasip1* mutants and suggest that paucity of cell number may partially be
141 compensated by the recruitment of additional cells into the sprout.
142

143 **Instability of tricellular junctions inhibits formation of multicellular tubes**

144 We next examined whether loss of *rasip1* affects angiogenic tube formation. In wild-
145 type embryos, the multicellular architecture of ISVs tubes is established via concerted
146 migratory and proliferative activities of endothelial cells. More specifically, the
147 multicellular configuration is driven by junctional rearrangements along the vessel axis,
148 which leads to effective cell pairing and thus multicellularity.

149 Since multicellular tubes are characterized and can be recognized by continuous
150 junctions along the blood vessel axis (Blum et al., 2008), we used a *ve-cad:ve-cad-*
151 *Venus* reporter (Lagendijk et al., 2017) to follow the dynamics of endothelial junctions
152 during ISV formation. In wild-type siblings, cell junctions elongated and spanned the
153 entire extend of the ISV giving rise to multicellular tubes by 48 hpf (Figure 2a, b, f).
154 Notably, adherens junctions maintained the continuity of the ISVs with the DA, where
155 they formed vertices or tri-cellular junctions (Figure 2a, white arrowheads). *rasip1*
156 mutants showed a clear delay in multicellular tube formation (Figure 2c) and at 48 hpf
157 – on average – about 40% of ISVs had not achieved a multicellular configuration
158 (Figure 2b). Moreover, time-lapse analysis of VE-cad-Venus showed defects in
159 junctional development (Figure 2a). Specifically, at the ventral base of the sprout,
160 junctions that were normally tethered to the DA in wild-type embryos, lost this
161 attachment and the junctional ring was "released" in mutant embryos (Figure 2a,
162 yellow arrowheads,d). This detachment resulted in one of the stalk cells moving up
163 into the DLAV leaving a single cell spanning the distance between the DA and the
164 DLAV (Figure 2a, e, f). These results indicate that junctional interconnections at the
165 base of the sprout are critical for cell intercalation to occur during multicellular tube
166 formation. Thus, the loss of these connections in *rasip1* mutant prevents cell pairing

167 and results in unicellular ISVs and consequently a defect in the cord hollowing process
168 underlying multicellular tube formation.
169
170 **Defects in junctional dynamics during blood vessel anastomosis**
171 The growth and interconnection of vascular networks requires angiogenic sprouting
172 as well as the interconnection of all sprout by the process of anastomosis. At the
173 cellular level, anastomosis occurs in a quite stereotyped fashion (reviewed by (Betz et
174 al., 2016). Neighboring sprouts initiate contact via tip cell filopodia and form a
175 junctional ring which surrounds apically polarized membrane. Junctional ring and
176 apical membrane formation in both of the contacting cells leads to the formation of a
177 luminal pocket, which is later connected to the lumen of the nascent vessel. The
178 process of anastomosis in zebrafish serves as a paradigm to study the cell biology of
179 blood vessel formation and includes processes such as apical polarization, junctional
180 rearrangements and lumen formation, which occur within a 4 to 6 hours (Herwig et al.,
181 2011). To assess the role of Rasip1 during anastomosis, we compared the dynamics
182 of junctional reporters such as VE-cad-Venus (Figure 3a) and Pecam-EGFP (S-Figure
183 3) in wild-type and mutant embryos. Time-lapse analyses revealed two different
184 defects in *rasip1* mutants during junctional ring formation. In about 50% of
185 anastomosis events (Figure 3a) we observed ectopic accumulation of VE-cadherin-
186 Venus or Pecam-EGFP (S-Figure 3) within the junctional ring, revealing a defect in
187 relocating these junctional proteins from the apical compartment to cell junctions.
188 Alternatively, in about 38% of cases, the anastomotic ring (Figure 3a) elongated along
189 the blood vessel axis but failed to maintain a lateral axis, leading to a collapsed
190 junctional ring.
191

192

193 The described defects were confirmed by immunofluorescent analysis of the junctional
194 proteins VE-cad, ZO-1 (tight junction protein 1, Tjp1) and Esama (endothelial-selective
195 adhesion molecule a) (Figure 3 d-e). In *rasip1* mutants VE-cad, Zo-1 as well as Esama
196 colocalized and formed reticulated junctions within the apical compartment. Together,
197 these observations indicate that Rasip1 plays a crucial role in the dynamic re-
198 localization of junctional components during *de novo* junction and lumen formation.

199

200 ***rasip1* mutants display transient intracellular luminal pockets**

201 As shown above *rasip1* mutant embryos display reduced vessel diameter and luminal
202 defects (Figure 1e-g). These luminal defects affect the onset of blood flow in the ISVs
203 (Figure 4a). We observed that initially unlumenized ISVs remained unlumenized at
204 least through day 4 of development (96 hpf) (Figure 4b). Moreover, in some instances
205 we observed that initially lumenized blood carrying ISVs collapsed in subsequent
206 stages (up to 96 hpf), indicating a role for Rasip1 in lumen maintenance (Figure 4b,
207 c). Thus, although luminal defects can be attributed to the inability of endothelial cells
208 to rearrange into a multicellular configuration (Figure 3), the above observations
209 suggest an additional defect in the formation or maintenance of a continuous luminal
210 compartment. This notion is supported by time-lapse analysis of ISV and DLAV
211 formation during lumen formation (Figure 5a). The timing of lumen formation in the ISV
212 is variable but usually starts between 30 and 32 hpf. In wild-type embryos we observed
213 that upon initiation, continuous lumens were formed within 30 minutes (Figure 5a). In
214 *rasip1* mutants, lumen formation was delayed and discontinuous. Instead, we often
215 observed luminal pockets in the dorsal aspects of the ISV (Figure 5a, yellow
216 arrowheads, S-Figure 5d). We surmised that luminal pockets could arise in three

217 different ways (Figure 5b) – either (1) by a collapse of a previously patent tube, (2) by
218 a local cord hollowing event, which failed to interconnect with other luminal pockets or
219 (3) by the formation of large intracellular vacuolar structures, which failed to fuse with
220 luminal membrane.
221
222 To differentiate between these scenarios, we performed a series of experiments. To
223 test whether luminal pockets may arise by lumen collapse, we performed
224 microangiography using a fluorescent tracer dye in 28 to 30 hpf embryos (Figure 5c).
225 Upon intravascular injection, the entire patent vasculature was labelled by quantum
226 dots. In *rasip1* mutants, however, we observed that although the base of the ISV was
227 positive for quantum dots, local luminal pockets in the DLAV were negative (Figure 5c,
228 yellow arrowheads). This strongly argues that luminal pockets in *rasip1* mutants arise
229 locally and do not represent luminal remainders formed by lumen collapse.
230
231 We next wanted to check whether luminal pockets represented intra- or extracellular
232 compartments. Extracellular luminal compartments arise between cells in a process
233 called cord hollowing, whereas intracellular lumens are thought to form by
234 vacuolation (Davis et al., 2011). During anastomosis in zebrafish embryos, cord
235 hollowing generates luminal pockets form as transient structures at the interface
236 between contacting tip cells (Blum et al., 2008). This interface is formed by a ring-
237 shaped junction, which surrounds an apical compartment of both tip cells (Herwig et
238 al., 2011). Thus, these extracellular pockets are demarcated by junctional rings,
239 while intracellular pockets should be outside of these rings. To test these
240 possibilities, we examined lumen formation in *rasip1* mutants expressing VE-cad-
241 Venus and found that they were located outside the junctional ring (Figure 5d

242 (00:12)), appearing as vesicular structures within the endothelial cytoplasm. Lateron
243 (Figure 6d (01:32)) these intracellular lumens were incorporated into the area
244 covered by the junctional ring, therefore representing transient structures. Taken
245 together, these findings show that loss of Rasip1 function leads to a transient
246 accumulation of intracellular vesicles, which later on merge into the anastomotic
247 compartment suggesting that Rasip1 may be critical for normal vesicle transport or
248 vesicle fusion during cord hollowing process, which occurs during anastomosis.
249

250 **Rasip1 localizes to apical membranes and endothelial cell junctions**

251 Our mutant analyses indicate a requirement for Rasip1 in junction formation and
252 remodeling, as well as in lumen formation and maintenance. To gain a better
253 understanding of how Rasip1 may be involved in these processes, we generated an
254 antibody against zebrafish Rasip1 to discern the subcellular localization of the protein
255 during angiogenesis. Immunofluorescent analysis confirmed endothelial expression of
256 Rasip1 in zebrafish embryos (S-Figure 4). Notably, Rasip1 protein levels appeared
257 dynamically regulated. During vasculogenesis, until the emergence of intersegmental
258 sprouts, Rasip1 was detected at high levels in the dorsal aorta (S-Figure 4a, b, yellow
259 arrowheads). In contrast, Rasip1 protein was highly expressed in sprouting ISVs while
260 it became downregulated in the dorsal aorta (S-Figure 4c, yellow bars), supporting the
261 notion that Rasip1 primarily functions during blood vessel morphogenesis rather than
262 during vessel maintenance. High-resolution imaging revealed specific subcellular
263 localization during blood vessel formation. In the context of anastomosis, three
264 different phases could be discerned. First, during contact formation (30 hpf), we found
265 that Rasip1 is absent from newly formed contacts (Figure 6a, yellow arrowheads).
266 However, Rasip1 was observed colocalizing with large junctional patches prior to

267 discernable formation of apical compartments. During later stages of anastomosis,
268 when the anastomotic ring had formed, Rasip1 was restricted to the apical
269 compartment within the junctional ring with no detectable Rasip1 at the junction
270 (Figure 6 b, yellow arrowheads). However, shortly later - during the establishment of
271 the DLAV (36 hpf) and later after full development of angiogenic vessels (48 hpf) - ,
272 we found that Rasip1 also localized to endothelial cell junctions (Figure 6c, white
273 arrowheads). Taken together, these studies show that Rasip1 dynamically distributes
274 during different phases of blood vessel formation. In particular, the dynamic subcellular
275 distribution to apical membrane compartments and endothelial cell junctions suggests
276 a sequential requirement for Rasip1 during apical compartment formation and
277 junctional remodeling, respectively.
278
279 Because of the early localization of Rasip1 to the apical membrane, we wanted to test
280 whether loss of Rasip1 function may affect apical polarization during blood vessel
281 formation. To this end, we generated a transgenic reporter (TG(EGFP-podxl)^{ubs29}),
282 which labels the apical membrane compartment (S-Figure 5). At 48 hpf, we observed
283 normal luminal localization of EGFP-Podxl in *rasip1* mutants (S-Figure 5). In ISVs that
284 displayed luminal defects, we observed slightly irregular distribution of EGFP-Podxl in
285 affected areas (enlarged insets in S-Figure 5). These observations suggest that in
286 spite of its apical localization, Rasip1 is not required for apical polarization in
287 endothelial cells.
288
289 **Overlapping requirement of Rasip1 and Radil-b in blood vessel formation**
290 Rasip1 protein has been shown to be an effector protein of the small GTPase Rap1
291 (Gingras et al., 2016). Protein binding studies have shown that Rasip1 can form

292 multimeric complexes consisting of Rap1, Rasip1, Radil (Ras-associating-dilute-
293 domain) and the GTPase-activating protein Arhgap29 (Post et al., 2013). Furthermore,
294 it has been shown that the core of these complexes can be formed by a Rasip1
295 homodimer or a Rasip1/Radil heterodimer (de Kreuk et al., 2016), indicating partly
296 overlapping functions of these proteins in endothelial cells. Rasip1 and Radil are
297 closely related proteins (S-Figure 5a) sharing several protein interaction domains such
298 as a Ras association (RA) domain conferring binding to Rap1, and a forkhead
299 association (FHA) domain binding the transmembrane receptor Heg1. An additional
300 PDZ domain is unique to Radil and is thought to interact with the GTPase-activating
301 protein Arhgap29 (Post et al., 2013). Radil function in endothelial cells has, so far, only
302 been addressed in cell culture experiments, which established its above-mentioned
303 protein interactions and indicated a role of Radil in endothelial barrier maintenance
304 and the regulation of endothelial cell adhesion (de Kreuk et al., 2016; Pannekoek et
305 al., 2014). Thus, we wanted to determine the role of Radil during blood vessel
306 morphogenesis *in vivo* and compare its requirement to that of Rasip1. The zebrafish
307 genome contains three *radil* paralogues, *radil-a,-b* and -*c*, respectively (S-Figure 5a).
308 Whole-mount in situ analysis revealed that of the three paralogues, only *radil-b* was
309 expressed specifically in endothelial cells (data not shown). Therefore, we analyzed
310 blood vessel formation in *radilb*^{sa20161} mutants, which carry a nonsense mutation
311 (Tyr129 → STOP) near the N-terminus of the protein (S-Figure 5b).
312 *radil-b* mutants were homozygous viable and could be raised to fertility. Nevertheless,
313 they exhibited several vascular defects similar to *rasip1* mutants, including cerebral
314 hemorrhages (S-Figure 5c), isolated luminal pockets (S-Figure 5d), reduction of blood
315 flow (S-Figure 5e) and retarded sprouting of ISVs (data not shown), supporting the
316 notion that both proteins are involved in the same molecular pathways. In contrast,

317 *radil-b* mutants did not phenocopy the junctional re-localization defect observed in
318 *rasip1* mutants during anastomosis (Figure 7a), suggesting that the proteins may also
319 have unique functions. *radil-b* mutants generally exhibited milder defects (S-Figure 5f,
320 g), in particular with respect to cellular architecture compared to single *rasip1* mutants
321 and *rasip1;radil-b* double mutants (Figure 7b). Furthermore, *rasip1;radil-b* double
322 mutants showed stronger sprouting and lumen formation defects than either single
323 mutant (Figure 7, S-Figure 5h), suggesting that while both proteins are required in this
324 process, they likely act in a partially redundant manner.
325

326 **Knock-down of *ccm1* and *heg1* phenocopies aspects of the *rasip1* mutant**

327 The Rasip1/Radil/Rap1 complex can bind via the FHA domain to the orphan
328 transmembrane receptor Heg1 (Gingras et al., 2016). This interaction has been shown
329 to tether Rasip1 to endothelial cell junctions (Post et al., 2013). To address the
330 relevance of this interaction during ISV morphogenesis, we analyzed *heg1* morphants
331 in order to test whether loss of Heg1 function showed any *rasip1*-like vascular
332 phenotypes. We also examined the phenotypes of *ccm1* morphants. Ccm1 binds to
333 Heg1 independently of Rasip1 (Gingras et al., 2012), and thus might indirectly
334 influence Rasip1 function. *ccm1* and *heg1* morphants exhibited blood vessel and heart
335 dilations as previously published (S-Figure 6a) (Hogan et al., 2008; Kleaveland et al.,
336 2009; Stainier et al., 1996). We consistently observed hemorrhages, which were less
337 pronounced than in *rasip1* mutants (Figure 8a and S-Figure 6b). However, similar to
338 *rasip1* mutants, ISV sprouting and development appeared to be delayed (Figure 8b).
339 To assess the role of Heg1 and Ccm1 in junctional rearrangements, we analyzed
340 endothelial cell junctions in transgenic VE-cad-Venus and Pecam1-EGFP reporter
341 background (S-Figure 6e). Consistent with earlier reports (Hogan et al., 2008;

342 Kleaveland et al., 2009), knock-down of *ccm1* or *heg1* did not cause obvious junctional
343 defects in the dorsal aorta. However, we observed detachment of junctions and
344 impaired cell rearrangements in sprouting ISVs (S-Figure 6c, d). In addition, it
345 appeared that Pecam-EGFP as well as VE-cad-Venus were not entirely cleared from
346 apical compartments during the formation of the DLAV.
347 To verify these observations, we performed immunofluorescent analyses to determine
348 whether endogenous VE-cadherin protein was cleared from the apical membrane
349 compartment in *heg1* and *ccm1* morphants. In both conditions, VE-cadherin
350 accumulated in the apical compartment embedded within the junctional rings – similar
351 to what we observed of *rasip1* mutants (Figure 8c). *In vivo* imaging of the junctions in
352 *ccm1* or *heg1* knock-down embryos showed a failure of multicellular vessel formation
353 (Figure 8d). Taken together, these findings show that *ccm1* and *heg1* loss-of-function
354 phenocopy defined aspects of *rasip1* mutants during critical aspects of blood vessel
355 formation during sprouting angiogenesis and anastomosis.
356

357 ## Discussion

358

359 Small GTPases of the Rho family play a key role in the regulation of cellular activities
360 during blood vessel formation. For example, they serve as molecular switches to
361 control cytoskeletal dynamics, cell adhesion and junction assembly during angiogenic
362 sprouting and lumen formation (Barlow and Cleaver, 2019). Rasip1 has been
363 described as an effector protein of small GTPase signaling during blood vessel
364 formation and maintenance (Koo et al., 2016; Wilson et al., 2013; Xu et al., 2011).
365 Rasip1 protein contains multiple protein binding domains and has been shown to
366 directly interact with its paralogue Radil, the small GTPase Rap1 and the

367 transmembrane protein Heg1 (de Kreuk et al., 2016; Gingras et al., 2016; Wilson et
368 al., 2013). By further association with proteins such as Arhgap29 and Ccm1, these
369 proteins control cortical actomyosin tension and endothelial junction formation and
370 dynamics (Post et al., 2015) and reviewed by (Lampugnani et al., 2017; Wilson and
371 Ye, 2014). Analyses of mutant mouse embryos have shown that Rasip1 is required
372 for proper lumen formation and maintenance in blood and lymphatic vessels (Koo et
373 al., 2016; Liu et al., 2018; Wilson et al., 2013). During vasculogenesis, Rasip1 is
374 required for the establishment of the nascent apical compartment and subsequently
375 for lumen expansion, presumably mediated by regulating Cdc42 and RhoA,
376 respectively (Barry et al., 2016).
377
378 **Multiple vascular defects in zebrafish *rasip1* mutants**
379 In order to gain a better understanding of how morphogenetic cell behaviors are
380 controlled by Rasip1, we generated loss-of-function mutants in the zebrafish *rasip1*
381 gene and analyzed these mutants focusing on cellular and junctional dynamics during
382 angiogenic sprouting and anastomosis. Overall, our findings are in agreement with
383 previously published vascular defects in mouse development, but also provide novel
384 insights into the regulation of junctional dynamics during angiogenic sprouting and
385 lumen formation.
386 *rasip1* mutants display numerous vascular defects, including cranial hemorrhage,
387 reduced blood circulation and reduced diameter of the dorsal aorta, consistent with
388 previously published *rasip1* knockdown experiments in zebrafish (Wilson et al., 2013).
389 Furthermore, we observe delayed angiogenic sprouting, as well as abnormalities in
390 lumen formation as well as impaired cell rearrangements, junctional dynamics and
391 stability. Despite this wide range of defects, the mutant phenotypes are consistent with

392 defects in the control of F-actin and junctional dynamics. The phenotypes of *rasip1*
393 mutants during vascular development are, however, quite distinct from those seen in
394 *ve-cad (cdh5)* mutants (Sauteur et al., 2014) indicating that Rasip1 is regulating
395 endothelial activities beyond cell junctions.
396
397 **Dynamic regulation of Rasip1 expression and subcellular localization**
398 Endothelial-specific expression of Rasip1 has been reported in several vertebrate
399 species including mouse, *Xenopus* and zebrafish, and Rasip1 appears to be
400 expressed in the entire embryonic vasculature (Wilson et al., 2013; Xu et al., 2009). In
401 contrast to its broad endothelial transcription, the distribution of Rasip1 protein
402 appears to highly regulated, with respect to the overall level and its subcellular
403 localization. During vasculogenesis, Rasip1 is readily detected at high levels in the
404 dorsal aorta, whereas at later stages expression is somewhat reduced. This
405 downregulation of Rasip1 in the dorsal aorta coincides with the commencement of
406 blood flow, suggesting that Rasip1 protein levels and localization may be controlled by
407 shear stress. The downregulation of Rasip1 protein in more mature vessels suggests
408 an essential role during blood vessel morphogenesis. In agreement with this, Rasip1
409 does not appear to be required in established blood or lymphatic vessels (Koo et al.,
410 2016; Liu et al., 2018).
411
412 During ISV sprouting we observe a shift of Rasip1 from the apical membrane
413 compartment during the early stages to higher levels at cell junctions during the later
414 stages of vascular tube formation. The early apical localization of Rasip1 is in
415 agreement with a previously proposed role in early apical-basal polarization, likely
416 upstream of Cdc42 (Barry et al., 2016). It will be important to determine how this

417 differential localization is accomplished or to what extend it reflects different functions
418 of Rasip1 during tubulogenesis. In *Drosophila*, it has been shown that apical
419 localization of canoe (the ortholog of vertebrate *afadin* and a homologue of rasip1) is
420 dependent on Rap1 (Bonello et al., 2018). Therefore, Rap1 is a putative candidate to
421 localize Rasip1 to apical membrane during vertebrate angiogenesis.
422
423 **A role for Rasip1 in angiogenic sprouting and blood vessel assembly**
424 Sprouting angiogenesis is accomplished by concerted endothelial cell dynamics
425 including cell migration, rearrangement, elongation and proliferation, all of which are
426 affected by the loss Rasip1 function. *rasip1* mutant ISVs contain fewer cells than wild-
427 type ISV, which reflects a reduced rate of cell proliferation during sprouting.
428
429 Furthermore, we observe a frequent failure of *rasip1* mutant ISVs to form multicellular
430 tubes. Formation of multicellular ISVs does not depend of the number of cells present
431 in the sprout (Angulo-Urarte et al., 2018) but rather relies on cell rearrangements
432 driven by junctional remodeling (Sauteur et al., 2014). For example, loss of VE-cad
433 prevents junction elongation and renders endothelial cells unable to move over each
434 other and effectively pair to form a multicellular tube (Paatero et al., 2018; Sauteur et
435 al., 2014). In *rasip1* mutants, however, the defect in cell pairing is caused by junctional
436 detachments. When we imaged VE-cad dynamics during ISV sprouting in wild-type
437 embryos, we found that, in many cases, two stalk cells maintain contact to the dorsal
438 aorta. In *rasip1* mutant sprouts, we observed that one of these cells detached from the
439 dorsal aorta and “retracted” to the dorsal part of the ISV, leaving the remaining cell
440 unpaired. Stalk cell detachment appears to occur at tri-cellular junctions indicating that
441 these junctions may be important as an anchor point to resist mechanical forces

occuring during cell rearrangements. A study performed in MDCK cells has shown that Afadin accumulates at tri-cellular junctions in response to tension (Choi et al., 2016). This finding supports the interesting notion that Rasip1 may play a specific role in reinforcing tri-cellular junctions during sprouting angiogenesis.

Rasip1 is required for lumen patency

Lumen formation in *rasip1* mutants is delayed and ISVs as well as the dorsal aorta show reduced vessel diameters during early embryonic development. At 48 hpf, we observed that about 50% of the ISVs were not patent and this defect was maintained at least through day 4 of development. Defects in luminal patency may have multiple causes. First, as described above, junctional detachment can prevent endothelial cell pairing and thus multicellular tube formation. Second, our examinations of the apical membrane using a Podxl-EGFP and Cherry-CAAX transgenic markers revealed an irregular shape of the apical membrane, suggesting luminal collapse. This observation agrees with earlier findings that Rasip1 regulates cortical actin tension during lumen opening of the dorsal aorta in mouse (Barry et al., 2016).

During the formation of the DLAV formation, we also observed luminal pockets, which did not label by microangiography and appeared outside of cell junctions, indicating that these lumens are intracellular and consist of large vesicles or vacuolar structures. Rasip1 has been shown to associate with early Rab5-positive and recycling Rab8-positive endosomes (Barry et al., 2016) and Rab8 has been implicated in the transport of Podocalyxin to the apical membrane in a Cdc42 dependent manner (Bryant et al., 2010). Further analyses will have to be undertaken to determine whether these

466 intracellular lumens are endosomal compartments and whether Rasip1 plays a role in
467 targeting recycling endosomes to the apical compartment.
468
469 **Rasip1 during anastomosis**
470 Vascular anastomosis is the process by which blood vessel connect and form a
471 network. Formation of the DLAV in the zebrafish is initiated by the interaction of two
472 neighboring tip cells which establish contact and form a localized *de novo* lumen at
473 their interface (Herwig et al., 2011) reviewed by (Betz et al., 2016). Formation of this
474 luminal pocket follows a relatively stereotyped sequence: upon initial interfilopodial
475 contact a junctional spot is formed, which is transformed into a ring surrounding apical
476 membrane. This spot to ring transformation entails the formation and expansion of a
477 stable junctional ring and the removal of junctional proteins from the center to permit
478 formation of an apical membrane compartment. Loss of Rasip1 prevents apical
479 clearance leading to ectopic junctions within newly formed apical compartments. A
480 similar phenotype has been observed in *Rasip1* mouse mutants during lumen
481 formation of the dorsal aorta and it was shown that this requirement is upstream of
482 Cdc42 (Barry et al., 2016). Thus, the molecular mechanisms driving apical clearance
483 during vasculogenesis and anastomosis appear to be rather conserved.
484
485 *In vitro* experiments have shown that Rasip1 localization at cell junctions requires its
486 interaction with the orphan receptor Heg1 (de Kreuk et al., 2016) and it has been
487 suggested that Rasip1 acts in concert with Heg1, Rap1 and Ccm1 and other proteins
488 in junction stabilization (reviewed by (Lampugnani et al., 2017)). To test whether
489 Rasip1, Ccm1 and Heg1 may interact during apical clearance, we performed
490 knockdown experiments. Knockdown of *ccm1* as well as *heg1* in zebrafish phenocopy

491 the apical clearance defects seen in *rasip1* mutants. Taken together, these data
492 suggest that some of the pathways which are involved in junction stabilization are also
493 required for or result in apical clearance during *de novo* lumen formation.
494 Rasip1, Radil and Arghap29 have been shown to form a complex and are thought to
495 regulate RhoA. Our analysis of *radil-b* and *rasip1/radil-b* double mutants has shown
496 that both proteins have similar functions during angiogenic sprouting and lumen
497 formation and maintenance. However, Radil-b appears to be dispensable for apical
498 junctional re-localization during anastomosis. In agreement with this interpretation,
499 studies in the mouse dorsal aorta have shown that clearance of apical junction
500 requires Cdc42 and is independent of RhoA (Barry et al., 2016).
501
502 In mouse dorsal aortae, loss of Rasip1 leads to an overactivation of Rock and an
503 increase of cortical actomyosin tension in the apical compartment (Barry et al., 2016).
504 As a consequence, the luminal surface of the endothelium cannot expand and the
505 lumen is constricted. In relation to this, we observe a collapse of the junctional ring
506 during anastomosis while the junctions are still maintained and elongate along the
507 vascular axis, resulting in a narrower apical compartment within the ring, eventually
508 leading to a close alignment of the junctions along the extending axis. We speculate
509 that this collapse of the junctional ring may be caused by an imbalance of the cortical
510 actin between apical and basolateral compartment, caused by an overactivation of
511 Rock at the apical side. Further studies on local actomyosin regulation will be required
512 to better understand the formation of a luminal surface during vasculogenesis and
513 vascular anastomosis.
514

515 # Materials and methods

516

517 **Zebrafish Strains and Morpholinos**

518 Zebrafish were maintained according to FELASA guidelines (Aleström et al., 2019).
519 All experiments were performed in accordance with federal guidelines and were
520 approved by the Kantonales Veterinäramt of Kanton Basel-Stadt. Zebrafish lines used
521 were *Tg(gata1a:DsRed)*^{sd2} (Traver et al., 2003), *Tg(kdrl:EGFP)*^{s843} (Jin, 2005),
522 *Tg(kdrl:EGFPnls)*^{ubs1} (Blum et al., 2008), *Tg(5xUAS:RFP)* (Asakawa and Kawakami,
523 2008), *Tg(fli1ep:gal4ff)*^{ubs3} (Herwig et al., 2011), *Tg(fli1a:Pecam-EGFP)*^{ncv27} (Ando et
524 al., 2016), *Tg(cdh5:cdh5-TFP-TENS-Venus)*^{uq11bh} (Lagendijk et al., 2017),
525 *Tg(UAS:EGFPpodxl)*^{ubs29} (this study) and *rasip1*^{ubs28} (this study) and *radilb*^{sa20161}
526 (European Zebrafish Resource Center, Karlsruhe, Germany). Morpholinos (Gene-
527 Tools, Corvallis, OR, USA) used were as follows:
528 *ccm1* 5'-GCTTTATTTCACCTCACCTCATAGG-3' (Mably, 2006),
529 *heg1* 5'-GTAATCGTACTTGCAGCAGGTGACA-3' (Mably et al., 2003),
530 standard control 5'-CCTCTTACCTCAGTTACAATTTATA-3'.

531

532 **Generation of *Tg(UAS:EGFPpodxl)*^{ubs29}**

533 The p5E-4xnrUAS promoter, pME-EGFP-podocalyxin (Navis et al., 2013) and p3E-
534 polyA (Kwan et al., 2007) were cloned into a Tol2 vector pDestTol2CG2 carrying
535 cmcl2:GFP to drive expression of GFP in the heart. The final plasmid was co-injected
536 with tol2 mRNA into the *Tg(fli1ep:gal4ff)*^{ubs3}*; (UAS:mRFP)* embryos. These mosaic
537 embryos were raised to adulthood and outcrossed with the parental fish line to
538 generate stable fish lines. The resulting *Tg(UAS:EGFPpodxl)* embryos were identified
539 on the basis of GFP expression in the heart; proper apical localization of EGFP-

540 Podocalyxin was confirmed using confocal microscopy. Two transgenic lines, ubs29
541 and ubs30, were isolated, and the ubs29 line showing more homogenous expression
542 levels in endothelium was used in experiments.
543
544 **Immunofluorescence**
545 Immunofluorescence was performed as previously described (Herwig et al., 2011).
546 The following antibodies were used: rabbit anti-zf-Cdh5 1:200 (Blum et al., 2008),
547 rabbit anti-Esama 1:200 (Sauteur et al., 2017), mouse anti-human-Zo-1 1:100
548 (Thermofisher), rabbit anti-Rasip1 1:500 (this paper), chicken anti-GFP 1:200
549 (Abcam), Alexa 405 goat anti-chicken immunoglobulin Y (IgY H&L) 1:1,000 (Abcam),
550 Alexa 568 goat anti-rabbit immunoglobulin G (IgG) 1:1,000, and Alexa 633 goat anti-
551 mouse IgG 1:1,000 (both from Thermofisher). The anti-zf-Rasip1 antibodies were
552 raised in rabbits against a synthetic peptide (CRTFLWGLDQDELPANQRTRL-COOH)
553 comprising the terminal amino acid residues (aa970-989) of the protein (Yenzym,
554 Antibodies LLC, Brisbane (CA, USA)).
555
556 **Live Imaging**
557 Time-lapse imaging was performed as previously described (Paatero et al., 2018). All
558 movies were taken with Leica SP5 or SP8 confocal microscopes using a 40x water
559 immersion objective (NA = 1.1) with a frame size of 1024x512 or 1024x1024 pixels.
560 Routinely, z stacks consisted of 80–100 slices with a step size of 0.8–1 μm. Stacks
561 were taken every 8- or 10-min. High-resolution imaging was performed a Zeiss
562 LSM880 microscope using a 40x water immersion objective (NA = 1.2) using a vertical
563 step size of 0.25 μm.
564

565 **Statistics**

566 Unless explicitly stated, all results shown were obtained from at least 3 independent
567 experiments, sample sizes were not predetermined, the experiments were not
568 randomized and investigators were not blinded to allocation during experiments and
569 outcome assessment. Statistical analyses were performed using Prism software
570 (GraphPad) and ordinary unpaired two-tailed Mann Whitney test.

571

572 ## Author Contributions

573

574 H.-G.B. and M.A. conceived the project; M.L. performed most experiments and
575 prepared the figures. C.B. generated *rasip1* mutant alleles and performed initial
576 experiments. N.S. characterized *radil-b* mutants; I.P. generated the
577 *Tg(UAS:EGFPpodxl)*^{ubs29} zebrafish line; C.W.W. and W.Y. provided the anti-zf-Rasip1
578 antibody; M.A and H.-G.B. supervised the project. M.L., M.A. and H.-G.B. wrote the
579 manuscript. All authors read and approved the manuscript.

580

581 ## Acknowledgements

582

583 We would like to thank the Biozentrum Imaging Core Facility for ceaseless support,
584 Li-Kun Phng and Gustavo Aguilar for critically reading the manuscript, Dr. Anne Karine
585 Lagendijk and Dr. Benjamin M. Hogan for providing the transgenic VE-cad-Venus
586 reporter , Dr. David Dylus for help on phylotypic analysis and Kumuthini Kulendra and
587 Mattias Thimm for fish husbandry. M.L. was supported by a fellowship from the
588 Werner-Siemens-Foundation (Zug). This work has been supported by the Kantons
589 Basel-Stadt and Basel-Land and by a grant from the Swiss National Science
590 Foundation to M.A.

591

References

Adams, R.H., Alitalo, K., 2007. Molecular regulation of angiogenesis and lymphangiogenesis. Nature Reviews Molecular Cell Biology 8, 464–478. doi:10.1038/nrm2183

Aleström, P., D'Angelo, L., Midtlyng, P.J., Schorderet, D.F., Schulte-Merker, S., Sohm, F., Warner, S., 2019. Zebrafish: Housing and husbandry recommendations. Lab Anim 51, 002367721986903–12. doi:10.1177/0023677219869037

Ando, K., Fukuhara, S., Izumi, N., Nakajima, H., Fukui, H., Kelsh, R.N., Mochizuki, N., 2016. Clarification of mural cell coverage of vascular endothelial cells by live imaging of zebrafish. Development 143, 1328–1339. doi:10.1242/dev.132654

Angulo-Urarte, A., Casado, P., Castillo, S.D., Kobialka, P., Kotini, M.P., Figueiredo, A.M., Castel, P., Rajeeve, V., Guasch, M.M.X., Millán, J., Wiesner, C., Serra, H., Muixi, L., Casanovas, O., als, F.V.X., Affolter, M., Gerhardt, H., Huveneers, S., Belting, H.-G., Cutillas, P.R., Graupera, M., 2018. Endothelial cell rearrangements during vascular patterning require PI3-kinase-mediated inhibition of actomyosin contractility. Nature Communications 1–16. doi:10.1038/s41467-018-07172-3

Asakawa, K., Kawakami, K., 2008. Targeted gene expression by the Gal4-UAS system in zebrafish. Develop. Growth Differ. 50, 391–399. doi:10.1111/j.1440-169X.2008.01044.x

Baeyens, N., Bandyopadhyay, C., Coon, B.G., Yun, S., Schwartz, M.A., 2016. Endothelial fluid shear stress sensing in vascular health and disease. J. Clin. Invest. 126, 821–828. doi:10.1172/JCI83083

Barlow, H.R., Cleaver, O., 2019. Building Blood Vessels—One Rho GTPase at a Time. Cells 8, 545–25. doi:10.3390/cells8060545

Barry, D.M., Koo, Y., Norden, P.R., Wylie, L.A., Xu, K., Wichaidit, C., Azizoglu, D.B., Zheng, Y., Cobb, M.H., Davis, G.E., Cleaver, O., 2016. Rasip1-Mediated Rho GTPase Signaling Regulates Blood Vessel Tubulogenesis via Nonmuscle Myosin II. Circ Res 119, 810–826. doi:10.1161/CIRCRESAHA.116.309094

Betz, C., Lenard, A., Belting, H.-G., Affolter, M., 2016. Cell behaviors and dynamics during angiogenesis. Development 143, 2249–2260. doi:10.1242/dev.135616

Blum, Y., Belting, H.-G., Ellertsdottir, E., Herwig, L., Lüders, F., Affolter, M., 2008. Complex cell rearrangements during intersegmental vessel sprouting and vessel fusion in the zebrafish embryo. Developmental Biology 316, 312–322. doi:10.1016/j.ydbio.2008.01.038

Bonello, T.T., Perez-Vale, K.Z., Sumigray, K.D., Peifer, M., 2018. Rap1 acts via multiple mechanisms to position Canoe and adherens junctions and mediate apical-basal polarity establishment. Development 145, dev157941–21. doi:10.1242/dev.157941

Bryant, D.M., Datta, A., Rodriguez-Fraticelli, A.E., Peränen, J., Martin-Belmonte, F., Mostov, K.E., 2010. A molecular network for de novo generation of the apical surface and lumen. Nat Cell Biol 12, 1035–1045. doi:10.1038/ncb2106

Choi, W., Acharya, B.R., Peyret, G., Fardin, M.-A., Mège, R.-M., Ladoux, B., Yap, A.S., Fanning, A.S., Peifer, M., 2016. Remodeling the zonula adherens in response to tension and the role of afadin in this response. The Journal of Cell Biology 213, 243–260. doi:10.1083/jcb.201506115

640 Davis, G.E., Stratman, A.N., Sacharidou, A., Koh, W., 2011. Molecular Basis for
641 Endothelial Lumen Formation and Tubulogenesis During Vasculogenesis and
642 Angiogenic Sprouting, 1st ed, International Review Of Cell and Molecular
643 Biology. Elsevier Inc. doi:10.1016/B978-0-12-386041-5.00003-0
644 de Kreuk, B.-J., Gingras, A.R., Knight, J.D., Liu, J.J., Gingras, A.-C., Ginsberg, M.H.,
645 2016. Heart of glass anchors Rasip1 at endothelial cell-cell junctions to support
646 vascular integrity. eLife 5, e11394. doi:10.7554/eLife.11394
647 Duran, C.L., Howell, D.W., Dave, J.M., Smith, R.L., Torrie, M.E., Essner, J.J.,
648 Bayless, K.J., 2017. Molecular Regulation of Sprouting Angiogenesis. Compr
649 Physiol 8, 153–235. doi:10.1002/cphy.c160048
650 Gebala, V., Collins, R., Geudens, I., Phng, L.-K., Gerhardt, H., 2016. Blood flow
651 drives lumen formation by inverse membrane blebbing during angiogenesis
652 in vivo. Nat Cell Biol 18, 443–450. doi:10.1038/ncb3320
653 Gingras, A.R., Liu, J.J., Ginsberg, M.H., 2012. Structural basis of the junctional
654 anchorage of the cerebral cavernous malformations complex. The Journal of Cell
655 Biology 199, 39–48. doi:10.1083/jcb.201205109
656 Gingras, A.R., Puzon-McLaughlin, W., Bobkov, A.A., Ginsberg, M.H., 2016.
657 Structural Basis of Dimeric Rasip1 RA Domain Recognition of the Ras Subfamily
658 of GTP-Binding Proteins. Structure/Folding and Design 24, 2152–2162.
659 doi:10.1016/j.str.2016.10.001
660 Herwig, L., Blum, Y., Krudewig, A., Ellertsdottir, E., Lenard, A., Belting, H.-G.,
661 Affolter, M., 2011. Distinct Cellular Mechanisms of Blood Vessel Fusion in the
662 Zebrafish Embryo. Current Biology 21, 1942–1948.
663 doi:10.1016/j.cub.2011.10.016
664 Hogan, B.M., Bussmann, J., Wolburg, H., Schulte-Merker, S., 2008. ccm1 cell
665 autonomously regulates endothelial cellular morphogenesis and vascular
666 tubulogenesis in zebrafish. Human Molecular Genetics 17, 2424–2432.
667 doi:10.1093/hmg/ddn142
668 Jin, S.W., 2005. Cellular and molecular analyses of vascular tube and lumen
669 formation in zebrafish. Development 132, 5199–5209. doi:10.1242/dev.02087
670 Kleaveland, B., Zheng, X., Liu, J.J., Blum, Y., Tung, J.J., Zou, Z., Sweeney, S.M.,
671 Chen, M., Guo, L., Lu, M.-M., Zhou, D., Kitajewski, J., Affolter, M., Ginsberg,
672 M.H., Kahn, M.L., 2009. Regulation of cardiovascular development and integrity
673 by the heart of glass–cerebral cavernous malformation protein pathway. Nature
674 Medicine 15, 169–176. doi:10.1038/nm.1918
675 Koo, Y., Barry, D.M., Xu, K., Tanigaki, K., Davis, G.E., Mineo, C., Cleaver, O., 2016.
676 Rasip1 is essential to blood vessel stability and angiogenic blood vessel growth.
677 Angiogenesis 1–18. doi:10.1007/s10456-016-9498-5
678 Kwan, K.M., Fujimoto, E., Grabher, C., Mangum, B.D., Hardy, M.E., Campbell, D.S.,
679 Parant, J.M., Yost, H.J., Kanki, J.P., Chien, C.-B., 2007. The Tol2kit: A multisite
680 gateway-based construction kit forTol2 transposon transgenesis constructs. Dev.
681 Dyn. 236, 3088–3099. doi:10.1002/dvdy.21343
682 Lagendijk, A.K., Gomez, G.A., Baek, S., Hesselson, D., Hughes, W.E., Paterson, S.,
683 Conway, D.E., Belting, H.-G., Affolter, M., Smith, K.A., Schwartz, M.A., Yap,
684 A.S., Hogan, B.M., 2017. Live imaging molecular changes in junctional tension
685 upon VE-cadherin in zebrafish. Nature Communications 1–12.
686 doi:10.1038/s41467-017-01325-6
687 Lampugnani, M.G., Dejana, E., Giampietro, C., 2017. Vascular Endothelial (VE)-
688 Cadherin, Endothelial Adherens Junctions, and Vascular Disease (2017). Cold
689 Spring Harbor Perspectives in Biology 9. doi:10.1101/cshperspect.a033720

690 Lawson, N.D., Weinstein, B.M., 2002. In Vivo Imaging of Embryonic Vascular
691 Development Using Transgenic Zebrafish. Developmental Biology 248, 307–318.
692 doi:10.1006/dbio.2002.0711
693 Lenard, A., Ellertsdottir, E., Herwig, L., Krudewig, A., Sauteur, L., Belting, H.-G.,
694 Affolter, M., 2013. In vivo analysis reveals a highly stereotypic morphogenetic
695 pathway of vascular anastomosis. Developmental Cell 25, 492–506.
696 doi:10.1016/j.devcel.2013.05.010
697 Liu, X., Gu, X., Ma, W., Oxendine, M., Gil, H.J., Davis, G.E., Cleaver, O., Oliver, G.,
698 2018. Rasip1 controls lymphatic vessel lumen maintenance by regulating
699 endothelial cell junctions. Development 145. doi:10.1242/dev.165092
700 Mably, J.D., 2006. santa and valentine pattern concentric growth of cardiac
701 myocardium in the zebrafish. Development 133, 3139–3146.
702 doi:10.1242/dev.02469
703 Mably, J.D., Burns, C.G., Chen, J.-N., Fishman, M.C., Mohideen, M.-A.P.K., 2003.
704 heart of glass Regulates the Concentric Growth of the Heart in Zebrafish. Current
705 Biology 13, 2138–2147. doi:10.1016/j.cub.2003.11.055
706 Navis, A., Marjoram, L., Bagnat, M., 2013. Cftr controls lumen expansion and
707 function of Kupffer's vesicle in zebrafish. Development 140, 1703–1712.
708 doi:10.1242/dev.091819
709 Paatero, I., Sauteur, L., Lee, M., Lagendijk, A.K., Heutschi, D., Wiesner, C.,
710 Guzmán, C., Bieli, D., Hogan, B.M., Affolter, M., Belting, H.-G., 2018. Junction-
711 based lamellipodia drive endothelial cell rearrangements in vivo via a VE-
712 cadherin-F-actin based oscillatory cell-cell interaction. Nature Communications
713 1–13. doi:10.1038/s41467-018-05851-9
714 Pannekoek, W.-J., Post, A., Bos, J.L., 2014. Rap1 signaling in endothelial barrier
715 control. Cell Adhesion & Migration 8, 100–107. doi:10.4161/cam.27352
716 Phng, L.-K., Gebala, V., Bentley, K., Philippides, A., Wacker, A., Mathivet, T.,
717 Sauteur, L., Stanchi, F., Belting, H.-G., Affolter, M., Gerhardt, H., 2015. Formin-
718 Mediated Actin Polymerization at Endothelial Junctions Is Required for Vessel
719 Lumen Formation and Stabilization. DEVCEL 32, 123–132.
720 doi:10.1016/j.devcel.2014.11.017
721 Post, A., Pannekoek, W.-J., Ross, S.H., Verlaan, I., Brouwer, P.M., Bos, J.L., 2013.
722 Rasip1 mediates Rap1 regulation of Rho in endothelial barrier function through
723 ArhGAP29. Proc. Natl. Acad. Sci. U.S.A. 110, 11427–11432.
724 doi:10.1073/pnas.1306595110
725 Post, A., Pannekoek, W.J., Ponsioen, B., Vliem, M.J., Bos, J.L., 2015. Rap1 Spatially
726 Controls ArhGAP29 To Inhibit Rho Signaling during Endothelial Barrier
727 Regulation. Molecular and Cellular Biology 35, 2495–2502.
728 doi:10.1128/MCB.01453-14
729 Sauteur, L., Affolter, M., Belting, H.-G., 2017. Distinct and redundant functions of
730 Esama and VE-cadherin during vascular morphogenesis. Development 144,
731 1554–1565. doi:10.1242/dev.140038
732 Sauteur, L., Krudewig, A., Herwig, L., Ehrenfeuchter, N., Lenard, A., Affolter, M.,
733 Belting, H.-G., 2014. Cdh5/VE-cadherin Promotes Endothelial Cell Interface
734 Elongation via Cortical Actin Polymerization during Angiogenic Sprouting.
735 CellReports 9, 504–513. doi:10.1016/j.celrep.2014.09.024
736 Stainier, D.Y., Fouquet, B., Chen, J.N., Warren, K.S., Weinstein, B.M., Meiler, S.E.,
737 Mohideen, M.A., Neuhauss, S.C., Solnica-Krezel, L., Schier, A.F., Zwartkruis, F.,
738 Stemple, D.L., Malicki, J., Driever, W., Fishman, M.C., 1996. Mutations affecting

739 the formation and function of the cardiovascular system in the zebrafish embryo.
740 Development 123, 285–292.
741 StriliC, B., KuCera, T., Eglinger, J., Hughes, M.R., McNagny, K.M., Tsukita, S.,
742 Dejana, E., Ferrara, N., Lammert, E., 2009. The Molecular Basis of Vascular
743 Lumen Formation in the Developing Mouse Aorta. DEVCEL 17, 505–515.
744 doi:10.1016/j.devcel.2009.08.011
745 Traver, D., Paw, B.H., Poss, K.D., Penberthy, W.T., Lin, S., Zon, L.I., 2003.
746 Transplantation and in vivo imaging of multilineage engraftment in zebrafish
747 bloodless mutants. Nat Immunol 4, 1238–1246. doi:10.1038/ni1007
748 Wilson, C.W., Parker, L.H., Hall, C.J., Smyczek, T., Mak, J., Crow, A., Posthuma, G.,
749 De Mazière, A., Sagolla, M., Chalouni, C., Vitorino, P., Roose-Girma, M.,
750 Warming, S., Klumperman, J., Crosier, P.S., Ye, W., 2013. Rasip1 regulates
751 vertebrate vascular endothelial junction stability through Epac1-Rap1 signaling.
752 Blood 122, 3678–3690. doi:10.1182/blood-2013-02-483156
753 Wilson, C.W., Ye, W., 2014. Regulation of vascular endothelial junction stability and
754 remodeling through Rap1-Rasip1 signaling. Cell Adhesion & Migration 8, 76–83.
755 doi:10.4161/cam.28115
756 Xu, K., Chong, D.C., Rankin, S.A., Zorn, A.M., Cleaver, O., 2009. Rasip1 is required
757 for endothelial cell motility, angiogenesis and vessel formation. Developmental
758 Biology 329, 269–279. doi:10.1016/j.ydbio.2009.02.033
759 Xu, K., Sacharidou, A., Fu, S., Chong, D.C., Skaug, B., Chen, Z.J., Davis, G.E.,
760 Cleaver, O., 2011. Blood vessel tubulogenesis requires Rasip1 regulation of
761 GTPase signaling. Developmental Cell 20, 526–539.
762 doi:10.1016/j.devcel.2011.02.010
763

764 # Figure legends

765

766 **Figure 1: vascular defects in zebrafish *rasip1* mutants. (a)** Conserved Rasip1
767 protein domains. RA: Ras association domain. FHA forkhead-association domain.
768 DIL: dilute domain. The *rasip1*^{ubs28} mutant allele consists of a 35kb deletion comprising
769 all three domains. **(b)** quantification of cranial hemorrhages in *rasip1*^{ubs28} mutant
770 embryos. p<0.0001 (Fisher's exact test). **(c)** confocal images of cranial hemorrhages
771 in rasip1^{ubs28} embryos (72 hpf). Blood cells are visualized by gata1:dsRed expression.
772 Scale bar, 50 µm . **(d)** bright field image of wild-type and *rasip1*^{ubs28} embryos showing
773 pericardial edema. Scale bar, 2 mm. **(e)** confocal images of wild-type and *rasip1*^{ubs28}
774 mutants. Mutants show narrower DA and irregular ISV diameters. Scale bar, 50 µm.
775 **(f)** quantification of DA diameters (µm) during embryonic development (32 to 120 hpf).
776 Mann Whitney test and error bars indicate standard deviation; significance (ns=not
777 significant, *p < 0.1). (WT 32, 48, 72, 120 hpf: *n*=4, 4, 9, 13 embryos; *rasip1*$^{ubs28/+}$ *n*=5,
778 12, 19, 33; *rasip1*^{ubs28} *n*=6, 10, 9, 10). **(g)** quantification of ISV diameters (µm) during
779 embryonic development (32 to 120 hpf). Embryos were analyzed by unpaired two-
780 tailed Mann Whitney test and error bars indicate standard deviation; significance
781 (ns=not significant, *p < 0.1, **p < 0.01, ****p < 0.0001). (WT 48, 72, 120 hpf: *n*=37,
782 94, 70 ISVs; *rasip1*$^{ubs28/+}$ *n*=104, 52, 198; *rasip1*^{ubs28} *n*=67, 38, 65).

783

784 **Figure 2: Formation of multicellular vessels is impaired in *rasip1* mutants. (a)**
785 Still pictures of time-lapse movies (s-movies 7 and 8) showing endothelial cell
786 junctions (Cdh5-Venus) in wild-type and *rasip1*^{ubs28} embryos. White arrowheads show
787 maintained junctional in wild-type ISV sprouts. Yellow arrowheads indicate junctional
788 detachment in mutant embryos. Scale bars, 20 µm. Bottom row: closeups of showing

789 junctional detachment in a^4 and a^5. **(b-e)** Quantification of junctional and cellular
790 configuration during ISV formation in wild-type and *rasip1*^{ubs28} mutant embryos. **(b)**
791 Percentage multicellular tubes at 48 hpf (wt *n*=8, mut *n*=6). **(c)** Speed of multicellular
792 tube formation (wt *n*=5, mut *n*=6). **(d)** Percentage of ISV with multicellular configuration
793 per embryo (WT *n*=4, mut *n*=5). **(e)** Percentage of single cell ISVs at 32 hpf (WT *n*=8,
794 mut *n*=8). Quantifications were done by counting ISVs showing the respective
795 phenotypes, averaged by total ISVs analysed per embryo. **(f)** Immunofluorescence of
796 Zo-1 and Esama in *Tg(kdrl:EGFP)*^{s843} at 32 hpf. Schematic drawings on the right show
797 the different cellular configurations of multicellular (wt) and unicellular (*rasip1* mutant)
798 ISVs. Scale bars, 5 µm. The data was analyzed by unpaired two-tailed Mann Whitney
799 test and error bars indicate standard deviation; significance (*$p < 0.1$, **$p < 0.01$).
800
801 **Figure 3: Requirement of Rasip 1 for dynamic re-localization of junctional**
802 **proteins and junctional ring formation during anastomosis. (a-c)** Still pictures of
803 time-lapse movies (s-movies 9-11) showing normal junctional patch to ring
804 transformation in wild-type (a) and abberant ring formation in *rasip1*^{ubs28} mutants (b,
805 c). Transgenic embryos expressing a VE-cadherin-Venus fusion protein were imaged,
806 starting at 30 hpf. Scale bar, 5 µm. **(d)** Immunofluorescence analysis of Zo-1 and VE-
807 cadherin in *Tg(kdrl:EGFP)*^{s843} at 32 hpf. *rasip1*^{ubs28} mutants show reticulated junctions
808 between two cells in the DLAV; wild-type embryo forms a cleared, ring-shaped
809 junction. Scale bars, 20 µm (overview) and 5 µm (inset). **(e)** Quantification of observed
810 junctional phenotypes at 32 hpf. *rasip1*^{ubs28} mutants show significant number of
811 reticulated junctions and collapsed anastomotic rings compared to wild-type (WT *n*=6
812 embryos, 53 analyzed rings, mut *n*=8, 68, Chi-Square: $p<0.0001$. **(f)**

813 Immunofluorescence analysis of Zo-1 and ESAMa in *Tg(kdrl:EGFP)*^{s843} at 32 hpf
814 showing a reticulated pattern in *rasip 1*^{ubs28} mutants . Scale bars, 5 µm.
815
816 **Figure 4: Protracted delays in lumen formation in rasip1 mutants. (a, b)** Live
817 images of *Tg(kdrl:EGFP)*^{s843}*; (gata1a:DsRed)*^{sd2} embryos. **(a)** Still images of a time-
818 lapse movies (s-movies 14, 15) starting at 30 hpf. **(b)** Tracking of individual
819 unlumenized ISV during embryonic development (32 to 96 hpf). Scale bars, 20 µm.
820 **(b)** % of blood carrying ISVs at 96 hpf (WT *n*=3 embryos, 28 analyzed ISVs, mut *n*=5,
821 46). Analyzed by unpaired two-tailed Mann Whitney test and error bars indicate
822 standard deviation; significance (*p < 0.1).
823
824 **Figure 5: Analysis of ectopic luminal pockets during DLAV formation in *rasip1***
825 **mutants. (a)** Still pictures of time-lapse movies (s-mov 16, 17) showing for the
826 emergence of ectopic luminal pockets (yellow arrowheads) in *rasip1* mutants. **(b)**
827 Schematic representation of possible cellular localization of ectopic lumens. To
828 differentiate between these possibilities two types of experiments: microangiography
829 (c) and colocalization of luminal pockets with junctional marker (d). **(c)** Visualization of
830 ectopic lumens and patent lumens in a *rasip1*^{ubs28} embryo (36 hpf). Ectopic luminal
831 pockets are indirectly visualized by the absence of cytoplasmic EGFP (yellow
832 arrowhead) (*Tg(kdrl:EGFP)*^{s843}). The patent lumen is marked by microangiography
833 using quantum dots in red (third panel in black). Ectopic lumens are not part of the
834 patent vasculature. **(d)** Still pictures of time-lapse movie (s-mov 18-21) during lumen
835 formation in the DLAV from around 32 hpf onward in wild-type (top) and *rasip1*^{ubs28}
836 (bottom) embryos. Endothelial cells are labeled with mRFP (greyscale images),

837 junctions are labeled by VE-cad-Venus (merged images). Yellow arrowheads indicate
838 the ectopic luminal pockets in *rasip1* mutants. Scale bar, 5 µm.
839
840 **Figure 6: Apical to junctional re-localization of Rasip1 during blood vessel**
841 **fusion. (a-e)** Immunofluorescent labeling of Rasip1 and Zo-1 during different stages
842 of DLAV formation (30 to 36 hpf). At 32hpf, Rasip1 is restricted to the apical surface
843 of the anastomotic ring (yellow arrowheads). At 36hpf, Rasip1 localizes to endothelial
844 junctions (Zo-1, white arrowheads). Scale bars, 5 µm
845
846 **Figure 7: Phenotypic comparison *of radil-b* single and of *rasip1/radil-b* double**
847 **mutants suggests partially overlapping functions during vascular**
848 **morphogenesis. (a)** Immunofluorescence analysis of Zo-1 and VE-cadherin
849 distribution in *Tg(kdrl:EGFP)*^{s843} at 32 hpf. **(b)** Live images at 48 hpf using *Tg(ve-*
850 *cad:ve-cadVENUS); Tg(fliep:gal4ff)*^{ubs3}*; (UAS:mRFP) reporter lines*. Scale bars: 5 µm
851
852 **Figure 8: Loss of Ccm1 and Heg1 phenocopies aspects of *rasip1* mutants. (a)**
853 Live images of Tg(kdrl:EGFP)^{s843};(gata1:Dsred)^{sd2} at 72 hpf. *ccm1* and *heg1*
854 morphants display mesenphalic hemorrhages while cranial circulation appears
855 completely disrupted. In addition, the MsV (Mesencephalic veins) and DLV (dorsal
856 longitudinal vein) (yellow arrowheads) are malformed. Scale bar, 50 µm. **(b)** Live
857 images of control, *ccm1* and *heg1* morphants at 32 hpf. *ccm1* and *heg1* morphants
858 show reduced DA diameters and defective ISV formation. Scale bar, 20 µm. **(c)**
859 Immunofluorescence analysis of control, *Ccm1* and *Heg1* morphants at 32 hpf.
860 Transgenic *Tg(kdrl:EGFP)*^{s843} embryos were stained for VE-cadherin. Scale bar, 5 µm.
861 **(d)** Quantification of multicellular ISVs at 48 hpf (Control MO injected embryos *n*=5,

862 24 analyzed ISVs; *Ccm1* MO *n*=4, 26; *Heg1* MO *n*=5, 23). Analyzed by unpaired two-
863 tailed Mann Whitney test and error bars indicate standard deviation; significance (**p
864 < 0.01).

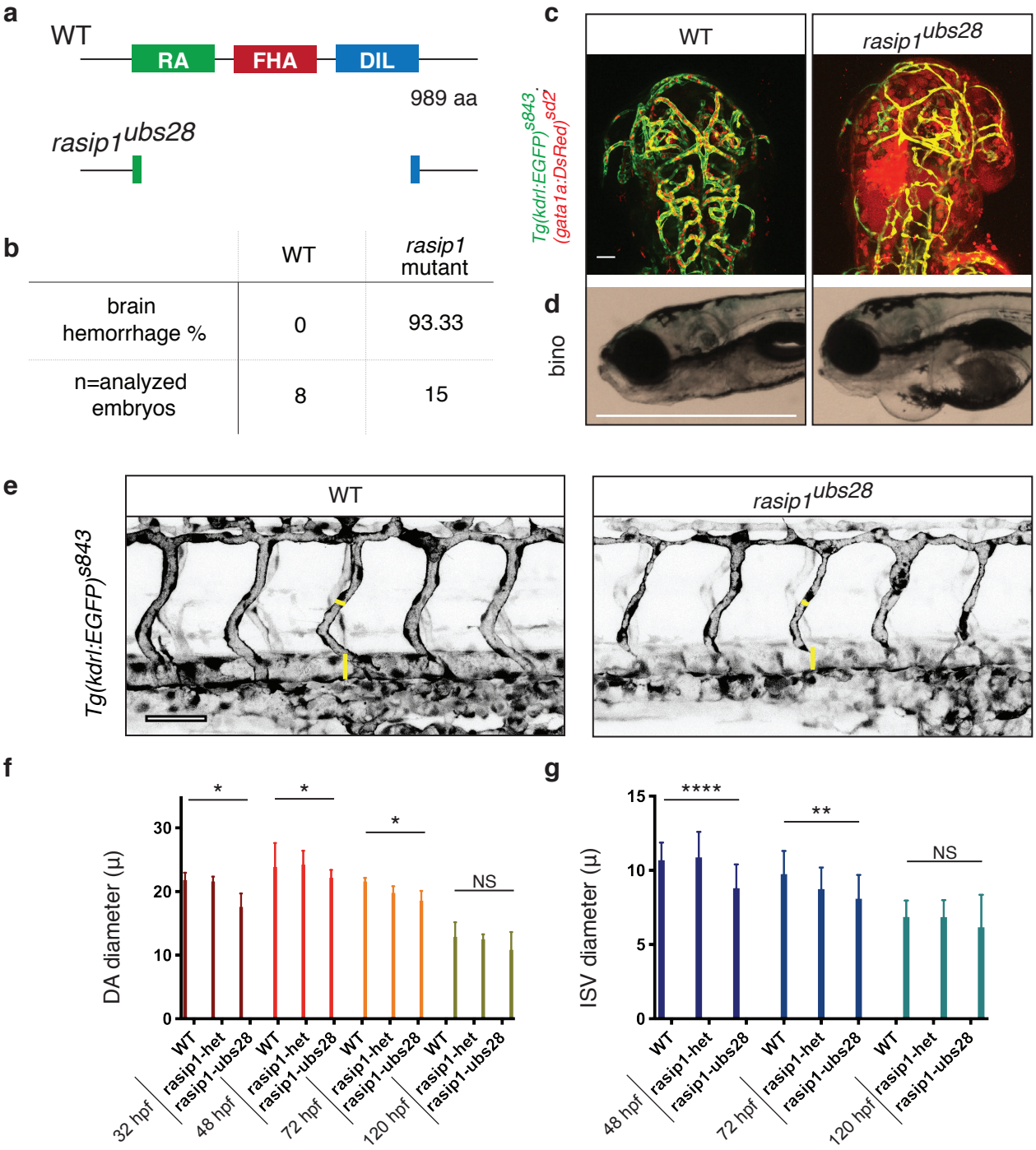
a
WT
RA
FHA
DIL
989 aa
rasip1ubs28
b
WT
rasip1 mutant
brain hemorrhage %
0
93.33
n=analyzed embryos
8
15
c
WT
rasip1ubs28
Tg(kdrl:EGFP)s843, (gata1a:DsRed)sd2
d
bino
e
WT
rasip1ubs28
Tg(kdrl:EGFP)s843
f
DA diameter (µ)
32 hpf
48 hpf
72 hpf
120 hpf
WT
rasip1-het
rasip1-ubs28
NS
g
ISV diameter (µ)
48 hpf
72 hpf
120 hpf
NS

Figure 1

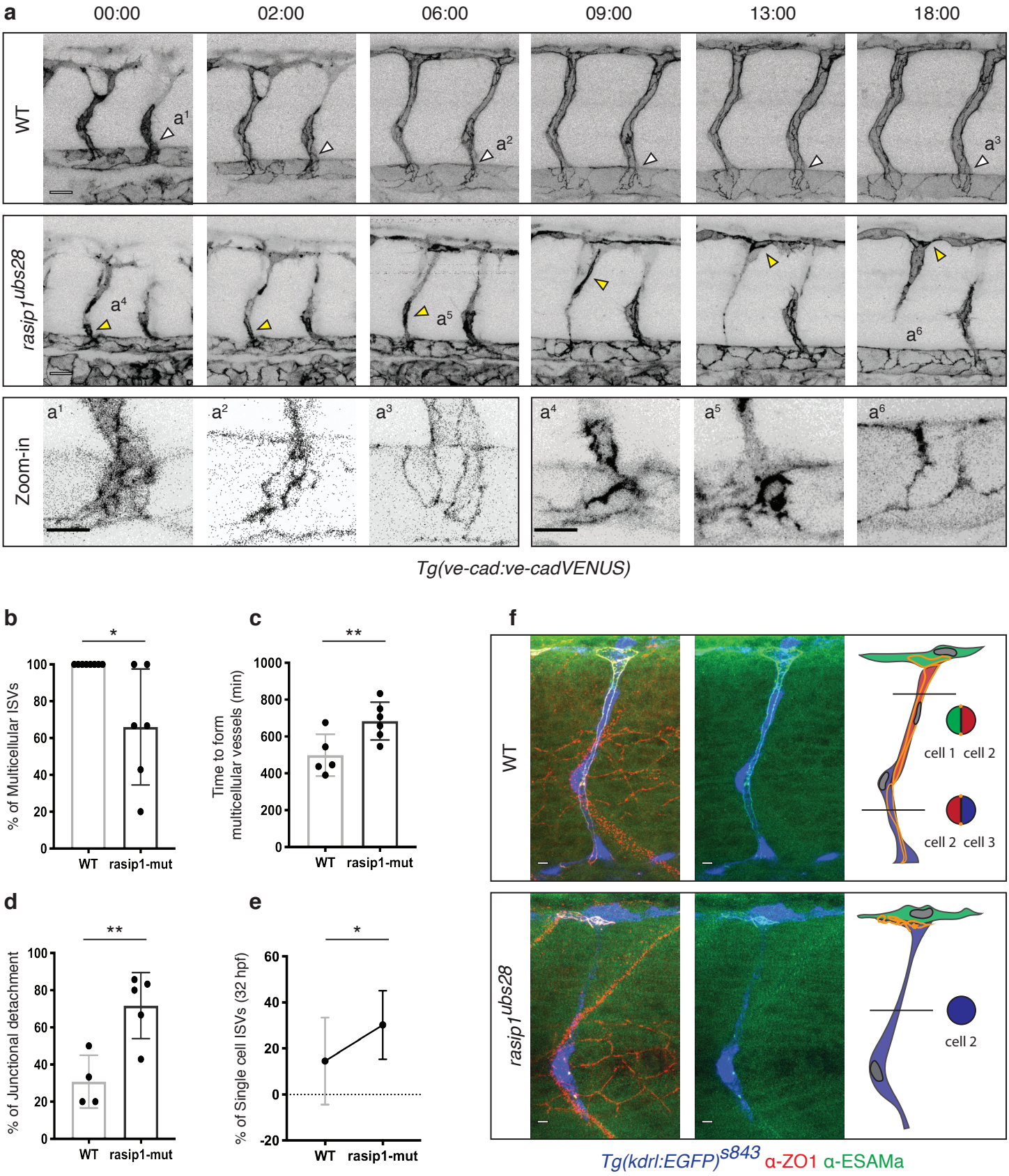
a
00:00
02:00
06:00
09:00
13:00
18:00
WT
rasip1ubs28
Zoom-in
a1
a2
a3
a4
a5
a6
Tg(ve-cad:ve-cadVENUS)
b
% of Multicellular ISVs
WT
rasip1-mut
c
Time to form multicellular vessels (min)
d
% of Junctional detachment
e
% of Single cell ISVs (32 hpf)
f
cell 1
cell 2
cell 3
Tg(kdrl:EGFP)s843 α-ZO1 α-ESAMa

Figure 2

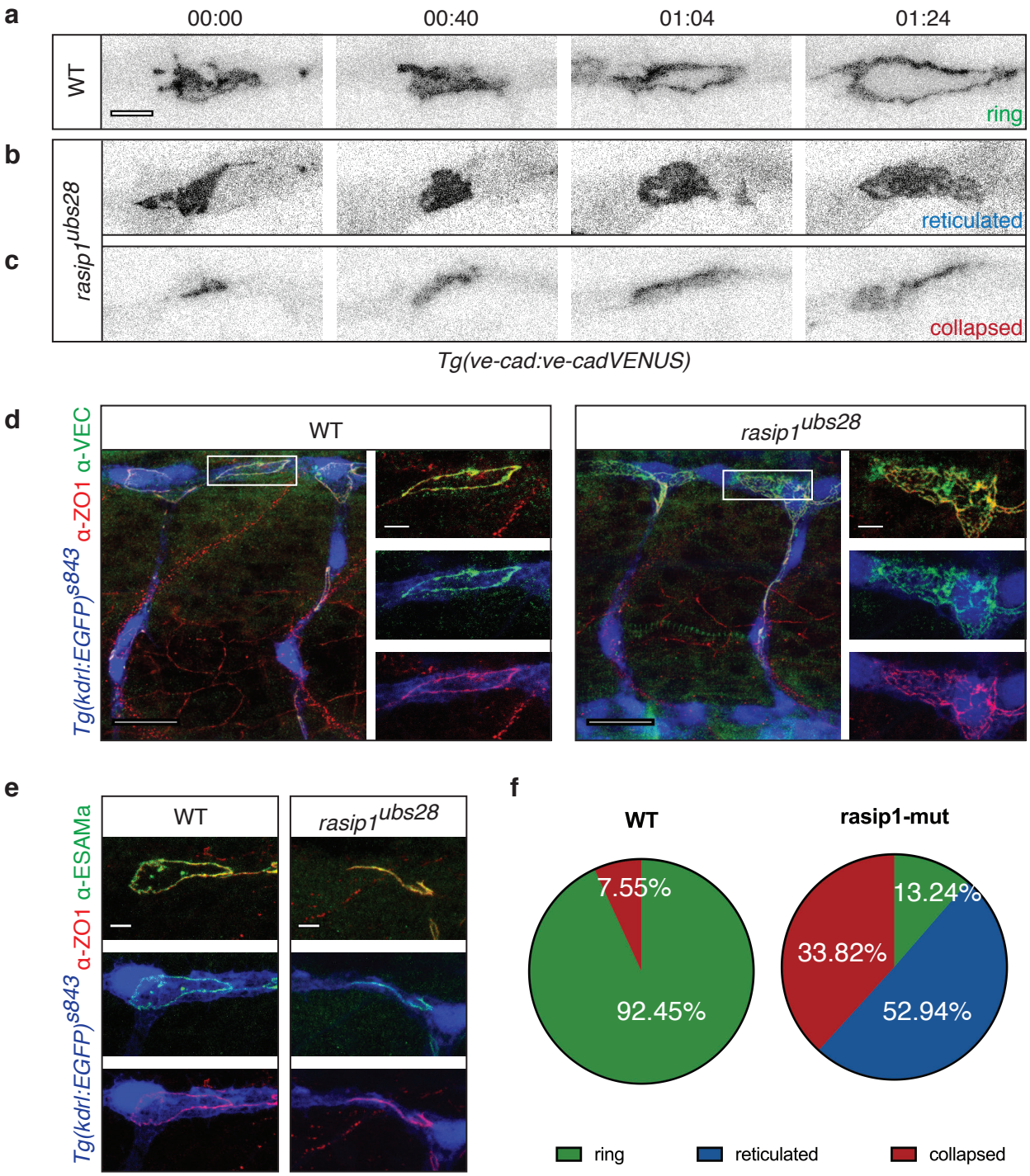
a
00:00
00:40
01:04
01:24
WT
ring
b
rasip1ubs28
reticulated
c
collapsed
Tg(ve-cad:ve-cadVENUS)
d
WT
rasip1ubs28
Tg(kdrl:EGFP)s843 α-ZO1 α-VEC
e
WT
rasip1ubs28
Tg(kdrl:EGFP)s843 α-ZO1 α-ESAMa
f
WT
rasip1-mut
7.55%
92.45%
13.24%
33.82%
52.94%
ring
reticulated
collapsed

Figure 3

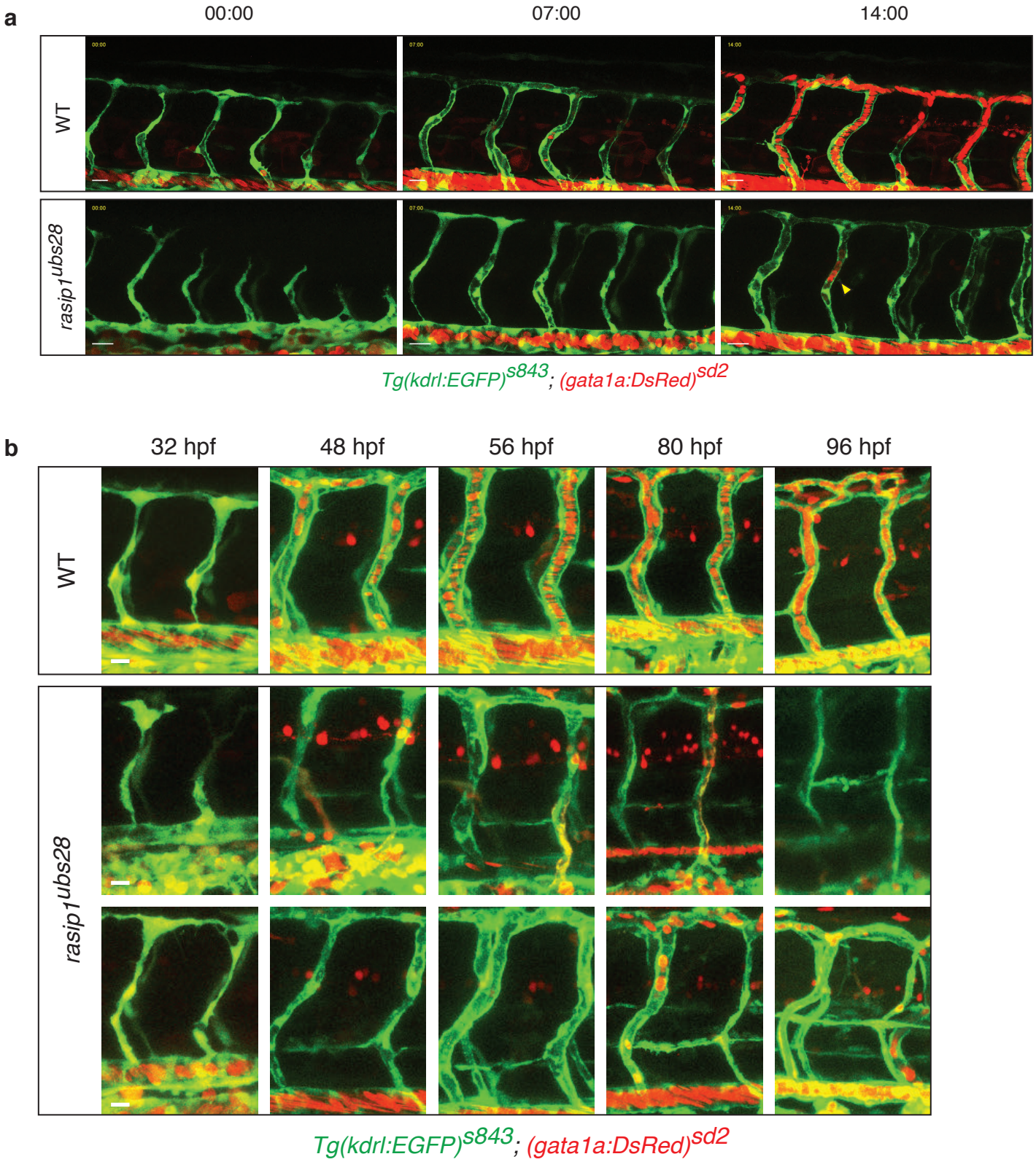
a
00:00
07:00
14:00
WT
rasip1ubs28
Tg(kdrl:EGFP)s843; (gata1a:DsRed)sd2
b
32 hpf
48 hpf
56 hpf
80 hpf
96 hpf
WT
rasip1ubs28
Tg(kdrl:EGFP)s843; (gata1a:DsRed)sd2

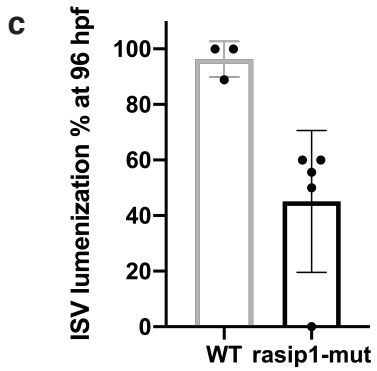
c
ISV lumenization % at 96 hpf
100
80
60
40
20
0
WT
rasip1-mut

Figure 4

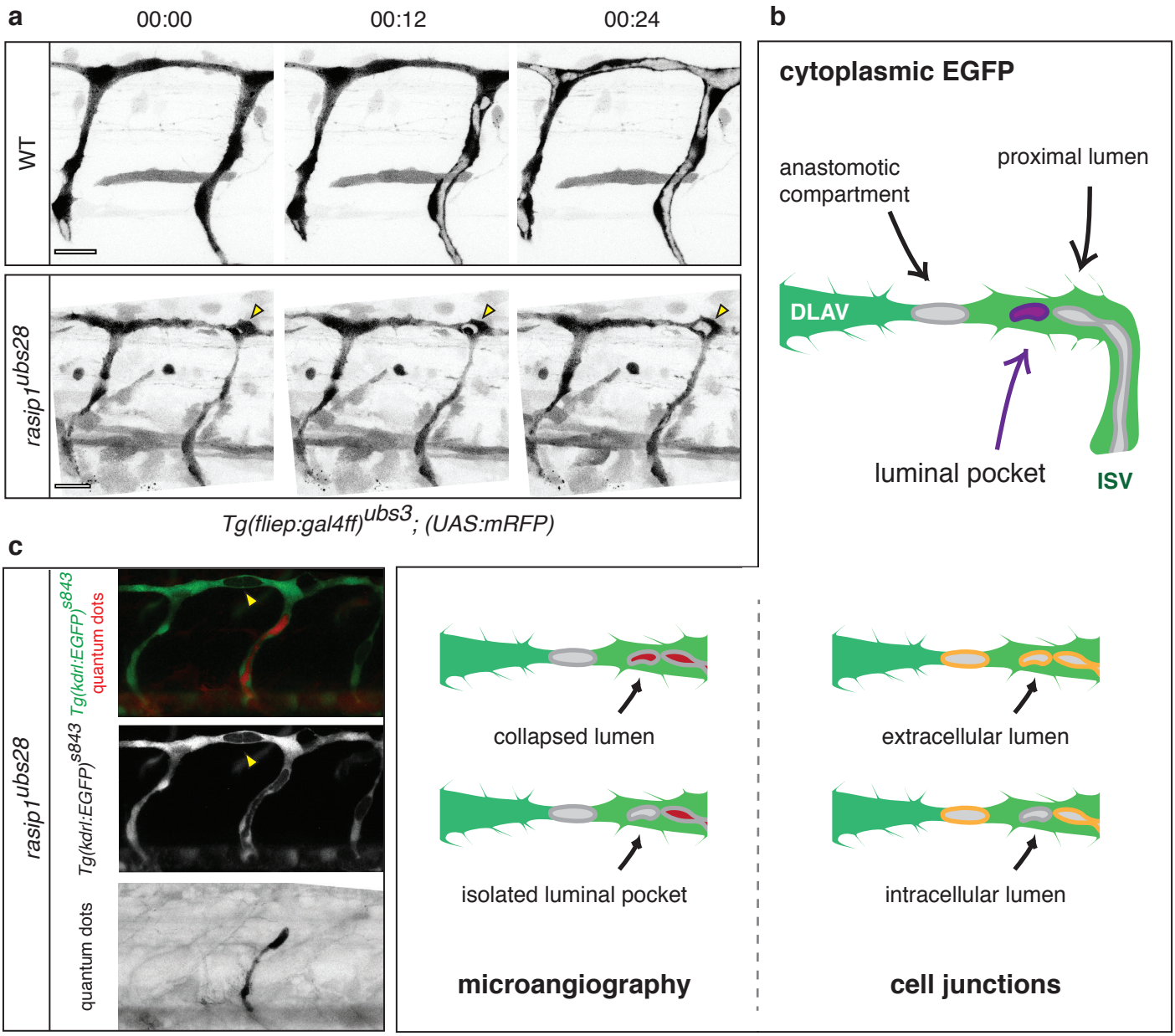
a
00:00
00:12
00:24
WT
rasip1ubs28
Tg(fliep:gal4ff)ubs3; (UAS:mRFP)
b
cytoplasmic EGFP
anastomotic compartment
proximal lumen
DLAV
luminal pocket
ISV
c
rasip1ubs28
Tg(kdrl:EGFP)s843
quantum dots
Tg(kdrl:EGFP)s843
quantum dots
collapsed lumen
isolated luminal pocket
microangiography
extracellular lumen
intracellular lumen
cell junctions

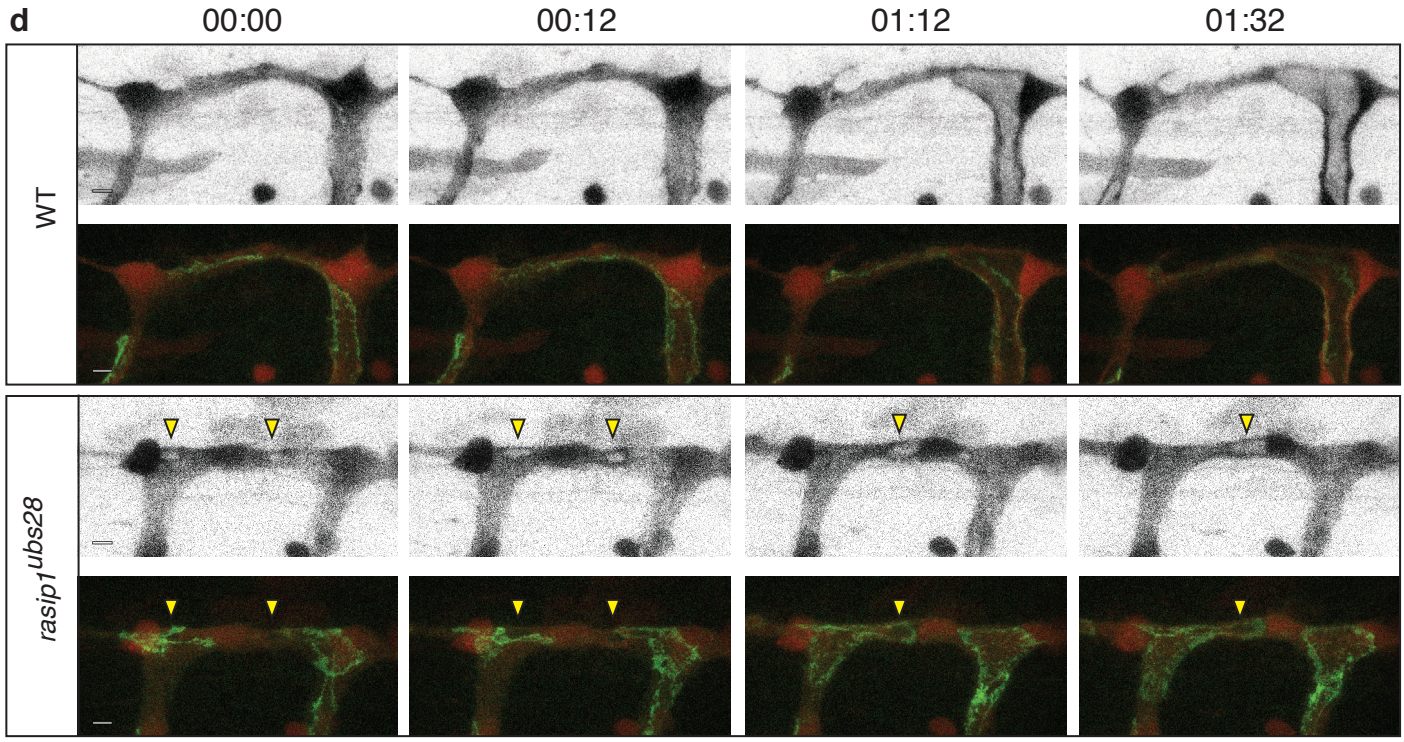
d
00:00
00:12
01:12
01:32
WT
rasip1ubs28
Tg(ve-cad:ve-cadVENUS); Tg(fliep:gal4ff)ubs3; (UAS:mRFP)

Figure 5

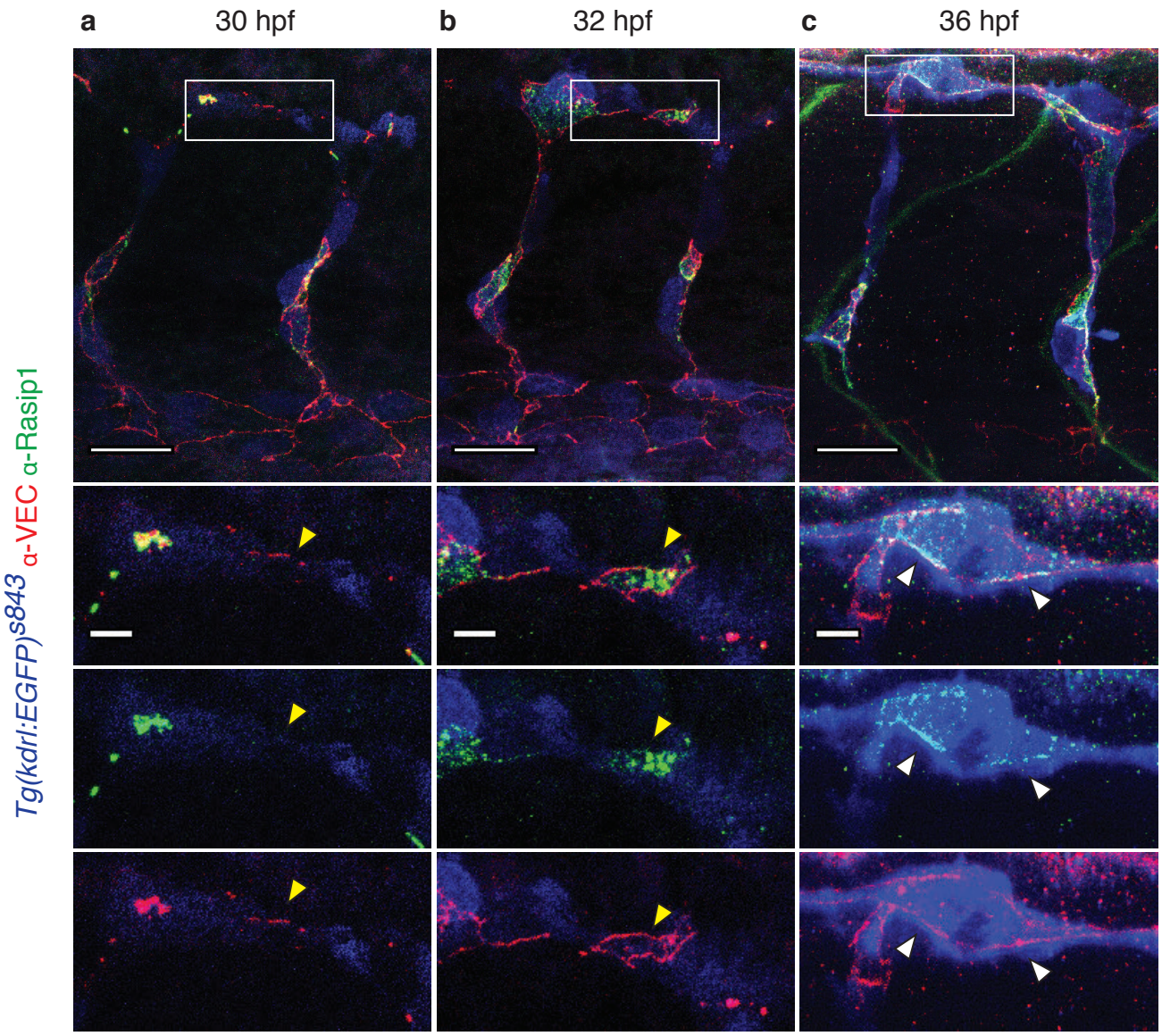

Figure 6

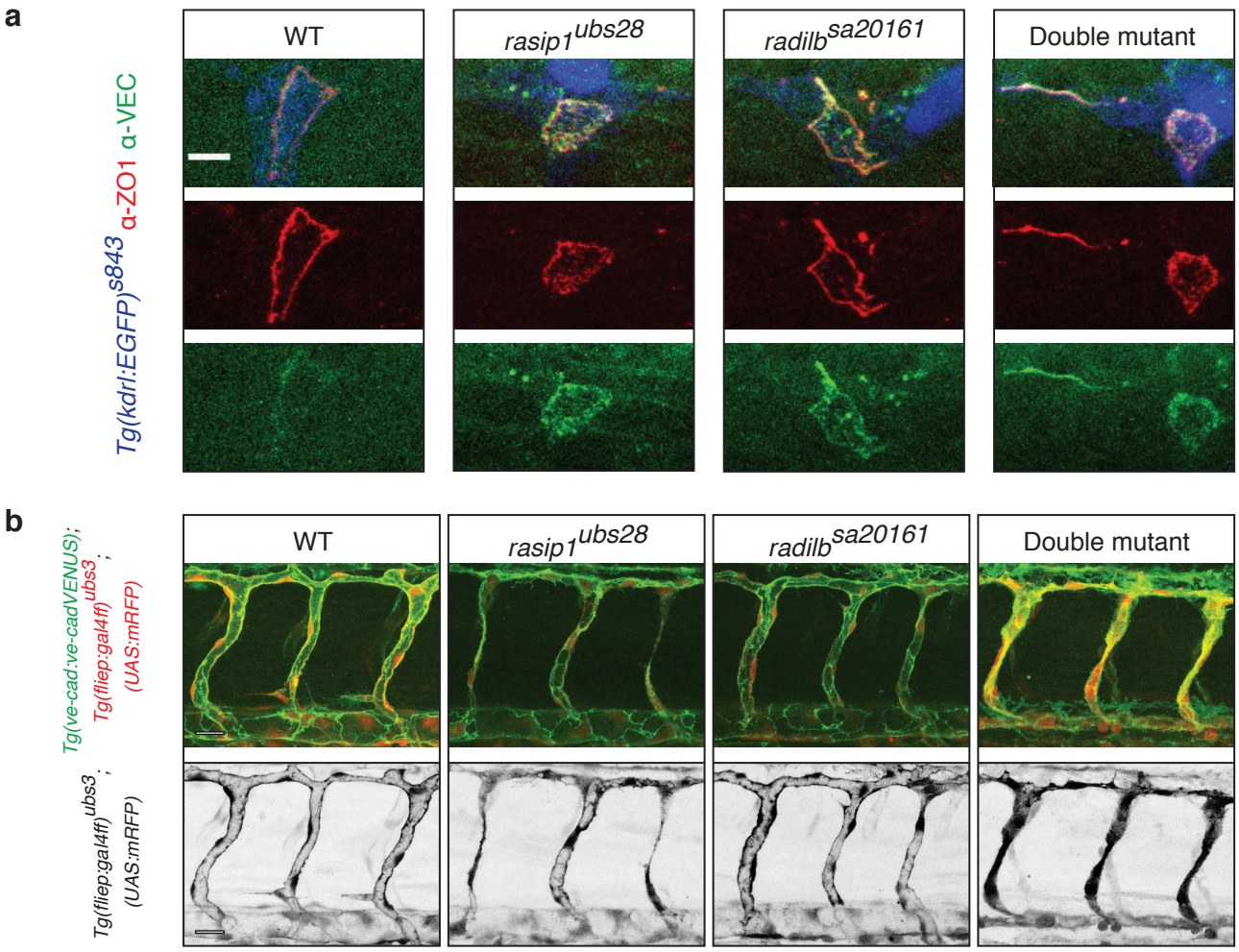
a
WT
rasip1ubs28
radilbsa20161
Double mutant
Tg(kdrl:EGFP)s843 α-ZO1 α-VEC
b
WT
rasip1ubs28
radilbsa20161
Double mutant
Tg(ve-cad:ve-cadVENUS); Tg(fliep:gal4ff)ubs3; (UAS:mRFP)
Tg(fliep:gal4ff)ubs3; (UAS:mRFP)

Figure 7

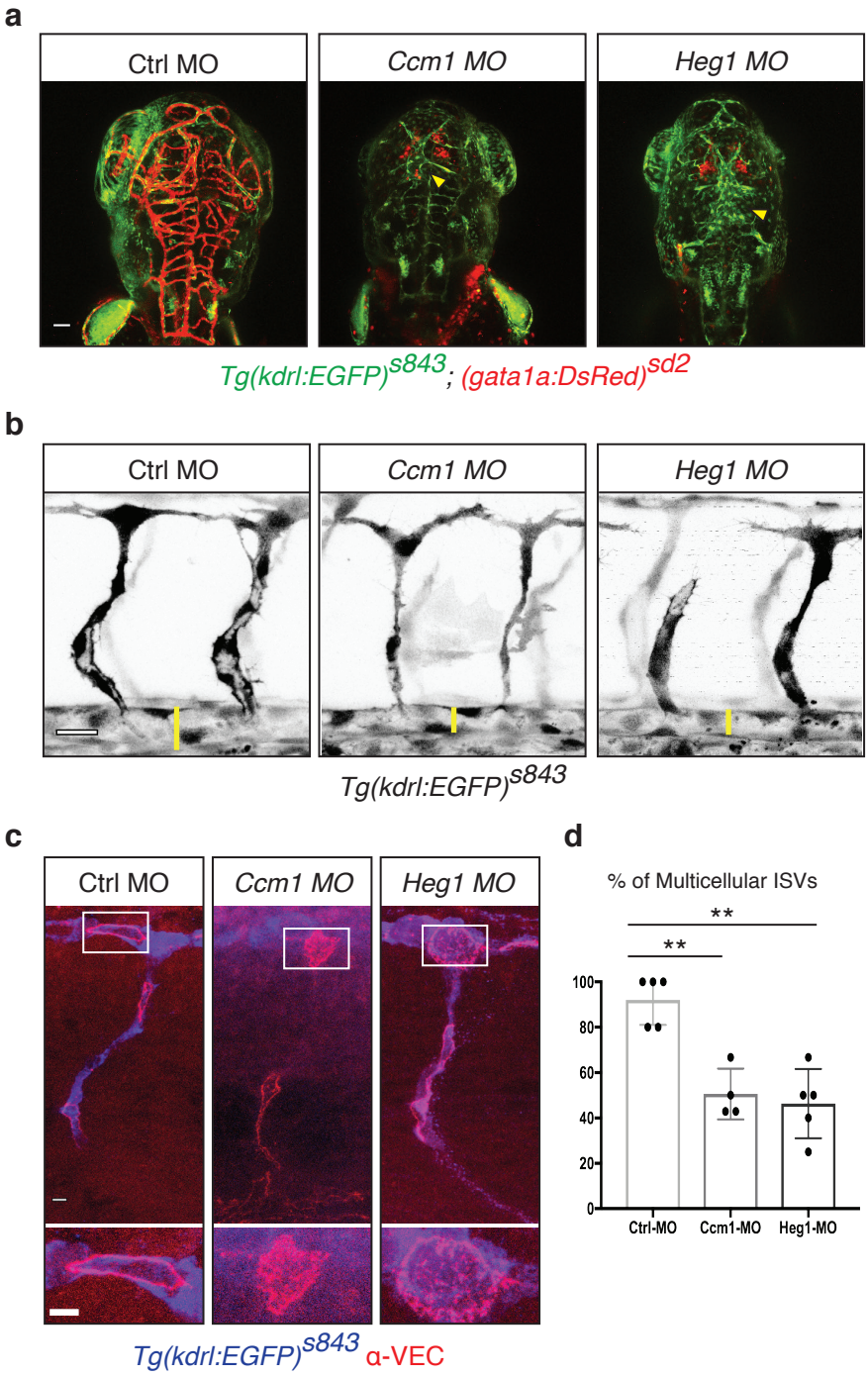
a
Ctrl MO
Ccm1 MO
Heg1 MO
Tg(kdrl:EGFP)s843; (gata1a:DsRed)sd2
b
Ctrl MO
Ccm1 MO
Heg1 MO
Tg(kdrl:EGFP)s843
c
Ctrl MO
Ccm1 MO
Heg1 MO
Tg(kdrl:EGFP)s843 α-VEC
d
% of Multicellular ISVs
**
**
100
80
60
40
20
0
Ctrl-MO
Ccm1-MO
Heg1-MO

Figure 8